Article

Not peer-reviewed version

Fourier-Transformation-Based Analysis of X-Ray Diffraction Pattern of Keratin for Cancer Detection

Alexander Alekseev , Oleksii Avdieiev , Sasha Murokh , Delvin Yuk , Alexander Lazarev , Daizie Labelle , Lev Mourokh * , Pavel Lazarev

Posted Date: 6 January 2025

doi: 10.20944/preprints202411.1739.v2

Keywords: X-ray diffraction; vitacrystallography; cancer detection; canine model; keratin; machine learning; Fourier transformation; ROC curves; principal component analysis

Article

Fourier-Transformation-Based Analysis of X-Ray Diffraction Pattern of Keratin for Cancer Detection

Alexander Alekseev [1,2], Oleksii Avdieiev [1], Sasha Murokh [1,3], Delvin Yuk [4], Alexander Lazarev [4], Daizie Labelle [4], Lev Mourokh [4,5,*] and Pavel Lazarev [1,4]

[1] Matur UK Ltd., 5 New Street Square, London EC4A 3TW, UK
[2] Department of Physics and Technology, Karaganda Buketov University, 100028 Karaganda, Kazakhstan
[3] Stuyvesant High School, 345 Chambers Street, New York, NY 10282, USA
[4] Arion Diagnostics, Inc., 911 Mustang Ct, Petaluma, CA 94954, USA
[5] Physics Department, Queens College, City University of New York, 65-30 Kissena Blvd, Flushing, NY 11367, USA
* Correspondence: lev.murokh@qc.cuny.edu

Abstract: As the number of cancer cases and deaths growing around the world, fast, non-invasive, and inexpensive screening is paramount. We examine the feasibility of such cancer detection using the X-ray scattering properties of nails in the canine model. 945 samples taken from 266 dogs were measured, with 84 animals diagnosed with cancer. To analyze the obtained X-ray diffraction patterns of keratin, we propose a method based on the two-dimensional Fourier transformation of the images. We compare 745 combinations of data preprocessing steps and machine learning classifiers and determine corresponding performance metrics. Excellent classification results are demonstrated, with sensitivity or specificity achieving 100% and the best value for balanced accuracy being 87.5%. We believe that our approach can be extended to human samples to develop a non-invasive, convenient, and cheap method for early cancer detection.

Keywords: X-ray diffraction; vitacrystallography; cancer detection; canine model; keratin; machine learning; Fourier transformation; ROC curves; principal component analysis

1. Introduction

Cancer remains one of the most serious problems of modern society, being the second-leading reason for mortality in the United States overall and the leading cause among people younger than 85 years. It is estimated [1] that in 2024, there will be more than two million new cases and more than six hundred thousand cancer-caused deaths in the US. The mortality rate has slightly decreased over the last few years [1], which can be attributed, in particular, to early diagnostics. To shift cancer detection further to early stages and achieve effective screening of large populations, the cancer research community has focused on biomarkers [2–5], i.e., cancer-induced changes in biochemical or molecular content. The biomarker tests are non-invasive and performed ex vivo, addressing the convenience and comfort of patients, but they are expensive and require significant time to process the results. The prominent alternative is screening structural biomarkers detected by X-ray diffraction (XRD).

Since its discovery [6,7], XRD has been a major tool in *crystallography*, uncovering the atom arrangements in crystalline solids. Diffraction patterns not only determine the symmetry of the crystal lattice but also reveal the electronic density at the lattice points, allowing the structure to be solved. The feasibility of enzyme crystallization [8] creates the pathway for *biocrystallography*. XRD on crystallized biological molecules deciphered the molecular content of complex structures; see [9] for historical overviews. Recently, it was shown that the X-ray scattering approach can be applied directly to biological tissues. This field of science, which we have called *vitacrystallography* [10],

 doi:10.20944/preprints202411.1739.v2

studies periodic structures in the extracellular matrix and their modifications induced by various diseases, especially cancer. Such modifications are detectable [11–15] and can lead to effective early cancer diagnostics. While most of the reports of cancer-induced changes are based on the alterations of X-ray scattering on lipids, the possibility of cancer detection using the keratin molecules of hair and nails was also discussed. Modifications associated with cancer in human hair were reported [16,17], but these measurements and their interpretations were disputed [18,19]. However, recent experiments [20] exhibited a high probability of cancer detection in dogs by the XRD patterns of their claws.

Studies of canine cancer are essential for two reasons. First, canines are excellent models since they spontaneously develop the same types of cancer as humans, leading to their use in comparative and translational oncology [21–23]. Second, 6 million pet dogs are estimated to be diagnosed with cancer in the United States [24], which puts an enormous burden on the animals and their owners. Early cancer detection is paramount for saving the lives of pets, and, at the same time, achievements in the canine model can be used to improve the treatment of human diseases. Comprehensive data can be collected from millions of dogs that visit the veterinary clinic each year, dramatically accelerating the development of new precision therapy that will benefit both dogs and their owners [24].

The potentially collected datasets require novel data representation and data analytics methods, including machine learning and artificial intelligence. Usually, for the XRD studies of biological tissue, the azimuthal integration is performed in the obtained two-dimensional (2D) image, and the data are represented in the intensity dependence on the momentum transfer q. This quantity corresponds to the scattering angle 2θ as $q = (4\pi \sin \theta)/\lambda$, where λ is the X-ray wavelength. This approach allows transparent physical interpretation of results because the momentum transfer is directly related to the periodicity d of molecular systems as $q = 2\pi/d$. In particular, XRD-based cancer detection [11–15] is related to specific features at 1.5 and 13.9 nm^{-1}, linked to the packing of triglycerides and inter-fatty-acid molecular distances, respectively [25]. However, a significant amount of information will be lost after the azimuthal integration for materials with angular anisotropy, such as keratin. The main goal of our paper is to develop a data analytic approach that avoids azimuthal integration and accounts for all the information contained in the XRD patterns.

In this work, we propose a method based on the 2D Fourier transformation of the XRD images and compare it to the previously developed 1D Fourier transformation approach [21]. We apply it to the dataset of 266 patients (dogs), with 104 of them diagnosed with cancer. As each dog provides more than one sample (cut from the claw), we have 945 XRD patterns, which we separated into the training (775 images) and test sets. We employ various data preprocessing steps, both standard and custom-developed, including Principal Component Analysis (PCA). Several machine learning algorithms are used to determine the performance metrics: Logistic Regression, Random Forest, Support Vector Machine, K-Nearest Neighbor, Naive Bayes Classifier, Light Gradient-Boosting Machine, and XGBoost. These first five classifiers are taken from the scikit-learn library [26,27], while the last two come from [28] and the XGBoost library [29,30], respectively. We obtain and compare the classification metrics for 745 combinations of the preprocessing steps and classifiers. These metrics are further improved if we group the samples from the same patient. For several combinations, either sensitivity or specificity reaches 1, and the balanced accuracy can be up to 0.875.

2. Materials and Methods

2.1. Sample Preparation

Samples from 266 patients (dogs) were collected, with 104 of them diagnosed with cancer. The patients are either client-owned animals of various breeds or beagles from a laboratory colony. The ages of the dogs ranged from 0.5 to 17 years. Patients provided several samples each (four for most), prepared and measured independently. The final dataset had 945 samples.

 doi:10.20944/preprints202411.1739.v2

The sample is a thin slice of hard outer shell tissue cut or shaved from the nail's surface. They are produced by a surgical knife to cut a very thin surface layer of the nail's outer hard shell with between 100 to 200 microns in thickness and an area of about 3 by 3 mm, as shown in Figure 1. It was shown previously that there was no visible difference between the samples obtained from dogs with and without cancer [20]. The samples were then placed into the specially designed holder, intended to hold the nail shaving under the X-ray beam, but no part of the sample holder would interact with the beam.

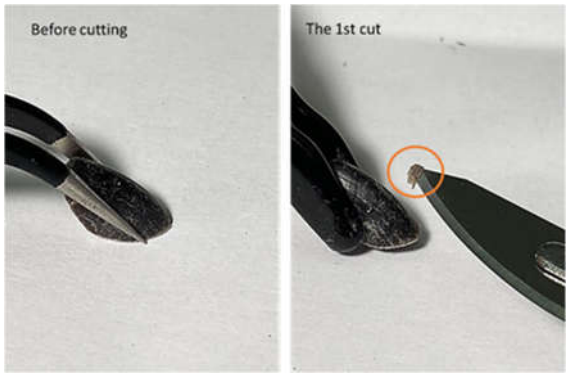

Figure 1. Left: The nail before cutting. Right: The surgical knife with the sample.

2.2. Diffraction Measurements

The custom-developed desktop X-ray diffractometer contains the beam delivery system, the sample receptacle, and the X-ray detector. We use the Xenocs X-ray source, a Genix 3D Cu with Fox 12–53 Cu Mirror, with a wavelength λ = 0.1540562 nm or energy of 8.04 keV. Xenocs also produced the focusing optics. The sample holder is placed on the receptacle, which includes a circular aperture beam collimator. The two-dimensional detector is an Advacam MiniPix SN1442 Si 500 μm with a 256-by-256-pixel array and a 55-by-55-micron pixel size. More details about our diffractometer can be found in Ref. [20]. The sample-to-detector distance for all samples was 13 mm, and the exposure time was 2 min. The samples were measured batch by batch; all results were obtained under the same experimental conditions. The experimental data were stored as 256-by-256 matrices of integers representing the photon counts. Each batch was complemented by at least one calibration file with silver behenate (AgBH) XRD patterns.

2.3. Data Analysis

2.3.1. Image Preprocessing

The raw XRD data were 2D images (256 × 256 pixels). Before further analysis, all images were preprocessed using the following steps:

1. Raw data was calibrated using silver behenate (AgBH) to unify scales for different batches. The image was rescaled during calibration to adjust the q-range to the same value. The calibrated image is shown in Figure 2(a).
2. The images were centered and rotated to unify the positions of essential features. The data were also cropped to a circular shape to make them symmetric.
3. Hot spots and hot pixels were removed, substituting them with the average intensity value over the circle with a certain radius.
4. The intensity of the diffracted beam was normalized, i.e., the total intensity of the preprocessed images was adjusted to 5 mln counts. The final preprocessed image is shown in Figure 2(b).

 doi:10.20944/preprints202411.1739.v2

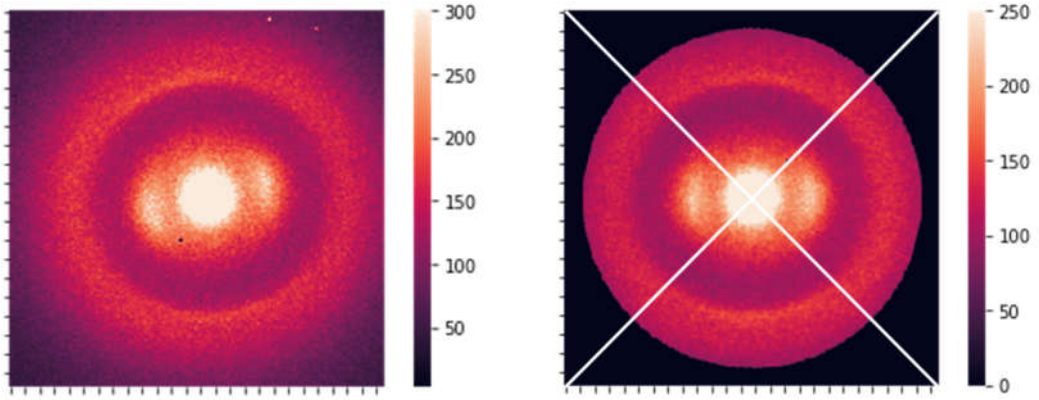

(**a**) (**b**)

Figure 2. The preprocessed XRD images: (**a**) The image after calibration; (**b**) The image after centering, rotation, removing hot pixels, and normalization.

2.3.2. One-Dimensional Fourier Transformation

The azimuthal integration of the two-dimensional dataset is performed to obtain the one-dimensional curve for subsequent determination of Fourier coefficients. We use two types of integration: (i) integration over 360 degrees (*AI*) and (ii) separate integrations over each of the four sectors (*AIS*) shown in Figure 2(b). These sectors contain either an arc or a peak (eye), corresponding to the pitch of chiral keratin molecules or the intermolecular distance in molecular packing [31]. The dependencies of the intensity on the momentum transfer q after the azimuthal integration are shown in Figure 3 for (a) 360 degrees, (b) sectors with eyes (horizontal, to the left and right of the primary beam), and (c) sectors with arcs (vertical, above and below the primary beam). Eyes and arcs produce characteristic features at 6.4 and 12.3 nm^{-1}, corresponding to 0.98 and 0.51 nm periodicities, respectively [31]. There is also a signal at 15.3 nm^{-1} originating from the 0.43 nm periodicity of the lipid structures. Orange and blue curves are the average for cancer and non-cancer patients. It is evident from this Figure that the cancer and non-cancer curves are very similar, and the two-dimensional analysis is essential for successful diagnostics.

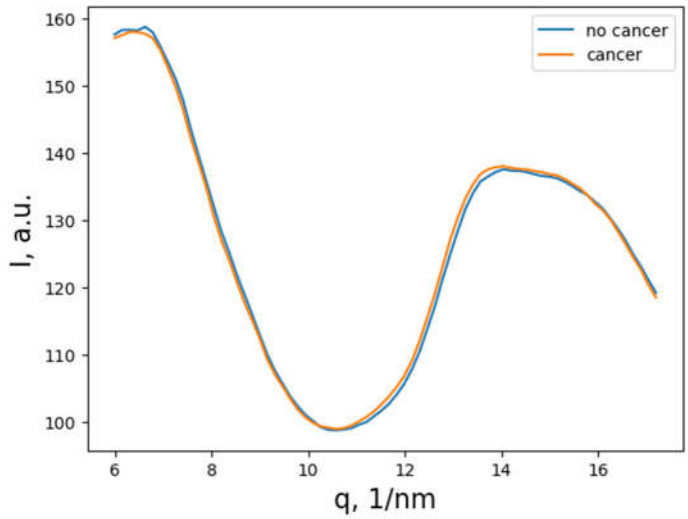

(**a**)

 doi:10.20944/preprints202411.1739.v2

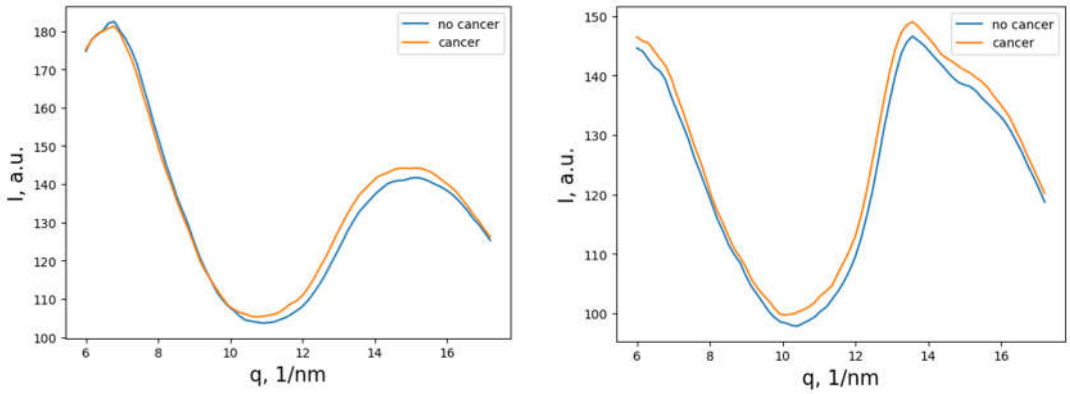

(**b**) (**c**)

Figure 3. Dependence of the intensity on momentum transfer after the azimuthal integration of the XRD patterns: (**a**) 360-degree integration; (**b**) Integration over the horizontal sectors; (**c**) Integration over the vertical sectors.

For the obtained dependencies of the intensity to the distance to the center, the regions close to the primary beam are cut, and the slope of the curve is removed for better Fourier series convergence (*SR*). One-dimensional Fourier coefficients are obtained via the Standard Discrete Fourier Transformation implemented in SciPy and NumPy libraries (*1DF*) or the custom procedure described in Ref. [20] (*1DFC*). We used Low Pass Fourier Filtration (*LPF*) to select only the most prominent low-frequency coefficients. Specifically, 30 coefficients were taken for AI curves or each of the four AIS curves.

2.3.3. Two-Dimensional Fourier Transformation

The two-dimensional (2D) Standard Discrete Fourier Transformation, implemented in SciPy and NumPy libraries, calculates the 2D Fourier coefficients (*2DF*). We used either the complete set (256 by 256 matrix) or 1257 complex Fourier coefficients obtained by the Low-Pass Fourier Filtering with the 20th-order cutoff. We tested different combinations of the Fourier coefficient components: real parts (*Re*), imaginary parts (*Im*), both real and imaginary parts (*Re_Im*), amplitudes (*Am*), and phases (*Ph*).

2.3.4. Additional Data Preprocessing Steps

Several optional steps can be taken for the data preprocessing. We can use the Standard Scaling procedure from the scikit-learn library [27] (*STD*) to standardize the contribution of features to the analysis and perform the Principal Component Analysis to reduce the number of variables. We exploit the following numbers of principal components: 3 (*PCA_3*), 50 (*PCA_50*), 100 (*PCA_100*), and 750 (*PCA_750*). We chose these values for the following reasons: 3 PCs can be visualized, 750 is close to the maximum possible number, 775 (the number of the samples in the training set), and 50 and 100 are the random numbers in between. The optimal number can be obtained via hyperparameter optimization, but it becomes increasingly computationally expensive for all the preprocessing steps and classifier combinations. As seen below, some classifiers perform better for 50 PCs, while others perform better at 100. Correspondingly, we have not performed further optimization and present only the results for these numbers.

Another optional step is the removal of the primary beam. It can be removed from the original images before the Fourier transformations (*BR*) or in the reciprocal space (*BRF*). For the latter, we introduced the following procedure. The auxiliary matrices are constructed with zeroes everywhere except the locations of the bright circles at the center. 2D Fourier transformations of these matrices contain the Fourier coefficients of the primary beam images. The differences between Fourier coefficients of original and auxiliary matrices are the coefficients of the beam-less XRD signal.

 doi:10.20944/preprints202411.1739.v2

The next step for all tasks is the preparation of the matrices for the machine-learning classifiers. These matrices have the dimensionality *M*x*N*, where *M* is the number of elements and *N* is the number of samples in the training set. For 2D cases where the Fourier coefficients are the matrices themselves, they are flattened, i.e., all the matrix elements are converted in a single row. In our studies, *N* = 775, while *M* changes from 30 for *1DF* to 1257 for the *LPF* and to 131,072 for *Re_Im* of the complete set of 2D Fourier coefficients.

2.3.5. Machine-Learning Classifiers

The classification algorithms applied in this work are related to supervised learning tasks [32]. One of the purposes of this work is to determine the most efficient classifiers for cancer diagnostics. Many different classification algorithms were used by research groups for medical diagnostics during the last decade [33,34], and it is still challenging to decide in advance which classifier will be most successful for experimental data. Here, we use the advantage of code organized through pipelines to compare various most popular classifiers. All applied classifiers form three main groups: simple and robust (Logistic Regression (*LR*), Support Vector Machine (*SVM*), K-nearest Neighbors (*KNN*), Gaussian Naïve Bayes (*GNB*)), bagging based algorithms (Random Forest Classifier (*RF*)) and boosting based algorithms (Extreme Gradient Boosting (*XGB*) and Light Gradient Boosting Machine (*LGBM*)). *LR* classifier fits training data by logistic function, which is then used for testing unseen data. *SVM* searches for optimal hyperplane, which separates classes in the space of features most efficiently. *KNN* utilizes the training dataset to make decisions on new unseen samples by assigning them to the most frequent class among k neighbors determined by distance metrics. *GNB* is based on Bayesian statistics and utilizes two main assumptions: independence of features and their Gaussian distribution. Random Forest classifier is one of the most popular and efficient machine learning methods [35]. It is an ensemble technique that creates a model by combining individual decision trees. Different decision trees are built using bagging, also called bootstrap aggregation. Only part of the data is used for single tree formation, providing a large variety of solutions. Then, the final decision is performed by voting, which improves the stability of the model with respect to random noise and overfitting. *XGB* and *LGBM* are ensemble machine learning techniques that will enhance model performance by ensemble weak prediction models [36]. Both gradient-boosting classifiers used in this work are decision-tree-based. The main difference between *RF* and gradient-boosting learners is that the latter connects trees in series and improves performance by reducing prediction errors of the previous iteration.

All classifiers used in this work have their advantages and limitations. For example, tree-based algorithms, *KNN* and *SVM*, are less influenced by outliers, and simple methods like *SVM* or *LR* are more interpretable. *GNB* is fast and efficient in classification, but the estimated cancer probability is unreliable. *LGBM* is faster and often more efficient than XGB due to different ways of tree construction (leaf-wise instead of level-wise used in XGB). We apply them to the same preprocessing steps to ensure an efficient comparison.

2.3.6. Pipeline Implementation

We use Visual Studio and Jupiter Notebook as the primary coding platforms. Our codes were written in Python using the machine learning library SciKitLearn [27], from which most classifiers were adopted, except gradient-boosting algorithms [28,30]. We have not performed the hyperparameter optimization in our code because it is computationally expensive for all the preprocessing steps and classifier combinations. However, the rough estimation of optimal hyperparameters for some models was performed manually and using the GridSearchCV function from the SciKitLearn library before final calculations. Some pipelines with too many features used in modeling require the Stochastic Gradient Descent (SGD) method [27] for reasonable computation time.

The main hyperparameters for classifiers were: maximal depth of trees max_depth for *RF* was not limited, and for *XGB* it was 3; the number of estimators for both *RF* and *XGB* was 15; and the

 doi:10.20944/preprints202411.1739.v2

number of neighbors k = 5 in *KNN*. The learning rate 'optimal' was used for *LR* and *SVM* with SGD training. The modeling process was implemented as a pipeline, where different preprocessing steps and classifiers were called in various combinations to determine the best algorithm for diagnostics.

3. Results

The measured XRD patterns were randomly separated into the training and testing datasets. The training dataset contains 132 non-cancerous and 84 cancerous patients (775 samples). The testing dataset has 30 non-cancerous and 20 cancerous patients. Both training and testing data were preprocessed using the same procedure. The training dataset optimized the model, and then the optimized estimator classified the testing dataset.

We used sensitivity (Sen_S), specificity (Spec_S), and balanced accuracy (BA_S) as performance metrics. Sensitivity is the proportion of the cancerous samples that were correctly identified. Similarly, specificity measures the proportion of non-cancerous samples that were correctly identified. Balanced accuracy = (specificity + sensitivity)/2. We also determine the receiver operating characteristics (ROC) curve and use the area under the ROC curve (AUC_S) as a metric. The results from the samples belonging to the same patient were averaged, and all performance metrics (Sen_P, Spec_P, BA_P, and AUC_P) were also calculated for the patients.

The best (in terms of BA_P) 10 combinations of the preprocessing steps and classifiers are shown in Table 1. The best results from the other approaches are presented in Table 2. The first column provides the total ranking. The second column describes the preprocessing steps and the classifier used, with the nomenclature taken from Section 2. Columns 3-6 show the metrics for the samples, and columns 7-10 demonstrate the metrics for patients.

Table 1. 10 best metrics for various preprocessing steps and classifiers.

	Steps and Classifiers	Sen_S	Spec_S	AUC_S	BA_S	Sen_P	Spec_P	AUC_P	BA_P
1	*2DF, BRF, LPF, STD, Im, PCA_100, RF*	0.61	0.95	0.85	0.78	0.75	1	0.93	0.875
2	*2DF, BRF, LPF, Am, LBGM*	0.63	0.96	0.82	0.79	0.85	0.9	0.92	0.875
3	*2DF, Re_Im, SVM*	0.72	0.88	0.86	0.8	0.8	0.93	0.91	0.865
4	*2DF, LPF, STD, Ph, PCA_50, SVM*	0.75	0.84	0.81	0.795	0.8	0.93	0.88	0.865
5	*2DF, LPF, Ph, SVM*	0.63	0.86	0.8	0.745	0.9	0.83	0.9	0.865
6	*2DF, BRF, LPF, STD, Re_Im, PCA_50, XGB*	0.6	0.88	0.81	0.74	0.85	0.87	0.89	0.86
7	*2DF, LPF, Ph, GNB*	0.72	0.86	0.78	0.79	0.75	0.97	0.86	0.86
8	*2DF, Ph, GNB*	0.73	0.82	0.78	0.775	0.7	1	0.88	0.85
9	*2DF, BRF, LPF, STD, Im, PCA_100, KNN*	0.58	0.98	0.79	0.78	0.7	1	0.84	0.85
10	*2DF, BRF, LPF, STD, Im, PCA_50, KNN*	0.58	0.98	0.79	0.78	0.7	1	0.84	0.85

Table 2. The best metrics for various preprocessing steps and classifiers not included in Table 1.

	Steps and Classifiers	Sen_S	Spec_S	AUC_S	BA_S	Sen_P	Spec_P	AUC_P	BA_P
13	*2DF, Am, LOG*	0.64	0.97	0.81	0.81	0.75	0.93	0.86	0.84
41	*AI, SR, 1DFC, RF*	0.94	0.43	0.75	0.685	1	0.63	0.87	0.815
42	*AIS, SR, 1DFC, RF*	0.79	0.69	0.8	0.74	0.9	0.73	0.88	0.815
53	*2DF, BRF, STD, Re, PCA_3, RF*	0.73	0.74	0.75	0.735	0.75	0.87	0.84	0.81

 doi:10.20944/preprints202411.1739.v2

118	*2DF, BRF, LPF, STD, Re_Im, PCA_750, RF*	0.69	0.6	0.68	0.645	0.85	0.73	0.8	0.79

One can see from these tables that the best diagnosis is obtained in two cases. The first is the Random Forest model based on imaginary parts of low-pass-filtered 2D Fourier coefficients with standard scaling and 100 principal components. The second is the Light Gradient Boosting Machine model based on amplitudes of low-pass-filtered 2D Fourier coefficients without PCA. The primary beam was removed in the reciprocal space for both cases. The proposed approach allows us to impose additional conditions on the search. Tables 3 and 4 show the best results with the conditions of specificity or sensitivity greater than 0.9. It should be noted that the same Random Forest model provided the best metrics in both cases.

Table 3. The best metrics for various preprocessing steps and classifiers with the additional condition that the ***sensitivity*** is greater than 0.9.

	Steps and Classifiers	**Sen_S**	**Spec_S**	**AUC_S**	**BA_S**	**Sen_P**	**Spec_P**	**AUC_P**	**BA_P**
1	*2DF, BRF, LPF, STD, Im, PCA_100, RF*	0.94	0.34	0.85	0.64	0.9	0.83	0.93	0.865
2	*2DF, LPF, Ph, SVM*	0.91	0.28	0.8	0.595	0.9	0.83	0.9	0.865
3	*2DF, Re_Im, SVM*	0.91	0.39	0.86	0.65	0.9	0.8	0.91	0.85
4	*2DF, BRF, LPF, Am, LBGM*	0.93	0.33	0.82	0.63	0.9	0.8	0.92	0.85
5	*2DF, BRF, LPF, STD, Im, PCA_100, XGB*	0.91	0.41	0.83	0.66	0.9	0.77	0.87	0.835

Table 4. The best metrics for various preprocessing steps and classifiers with the additional condition that the ***specificity*** is greater than 0.9.

	Steps and Classifiers	**Sen_S**	**Spec_S**	**AUC_S**	**BA_S**	**Sen_P**	**Spec_P**	**AUC_P**	**BA_P**
1	*2DF, BRF, LPF, STD, Im, PCA_100, RF*	0.61	0.95	0.85	0.78	0.75	1	0.93	0.875
2	*2DF, BRF, LPF, Am, LBGM*	0.63	0.96	0.82	0.79	0.85	0.9	0.92	0.875
3	*2DF, Re_Im, SVM*	0.72	0.88	0.86	0.8	0.8	0.93	0.91	0.865
4	*2DF, LPF, STD, Ph, PCA_50, SVM*	0.75	0.84	0.81	0.795	0.8	0.93	0.88	0.865
5	*2DF, LPF, Ph, GNB*	0.72	0.86	0.78	0.79	0.75	0.97	0.86	0.86

Comparing the ROC curves can provide additional information. In Figure 4, we present four characteristic curves for patients.

 doi:10.20944/preprints202411.1739.v2

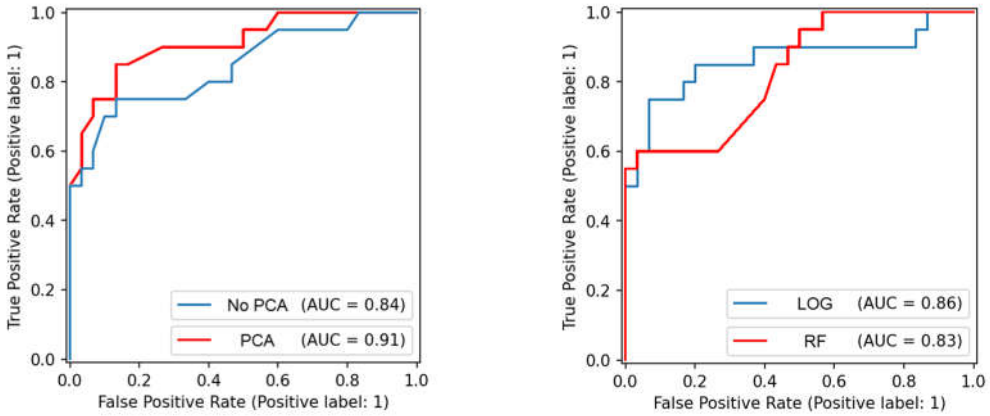

(**a**) (**b**)

Figure 4. ROC curves for various preprocessing steps and machine learning algorithms (the terminology is described in Section 2): (**a**) *2DF*, *LPF*, *BRF*, *Im*, and *RF* (*STD* and *PCA_100* for the red curve, no *STD* and *PCA_100* for the blue curve); (**b**) *2DF* and *Am* (*LOG* for the blue curve and *RF* for the red curve).

In Figure 4(a), we present the red ROC curve for the best-performing combination of the data preprocessing steps and machine learning algorithms: Random Forest model based on imaginary parts of low-pass-filtered 2D Fourier coefficients with standard scaling, 100 principal components, and the primary beam removed in the reciprocal space. Almost the same combination but without standard scaling and principal components produces the blue ROC curve of this figure, with much worse metrics. Figure 4(b) compares the results of two different classifiers for the amplitudes of the complete set of 2D Fourier coefficients without beam removal, standard scaling, and principal component analysis. The Logistic Regression (in blue) produces a larger AUC than the Random Forest (in red). The balanced accuracy for *LOG* is also larger (0.84 vs. 0.78), although the results are the opposite for the specificity (0.93 vs. 0.97). It should be noted that this is the only case where the results of the Logistic Regression are comparable to those of other classifiers. Usually, they are much worse.

Another type of visualization is representing data in the space of principal components. We use it in Figure 5 to compare two approaches to primary beam elimination. This figure shows the data corresponding to the amplitudes of low-pass-filtered 2D Fourier coefficients after the standard scaling, but for Figure 5(a), the beam was removed in the reciprocal space, while for Figure 5(b), it was done in the real space.

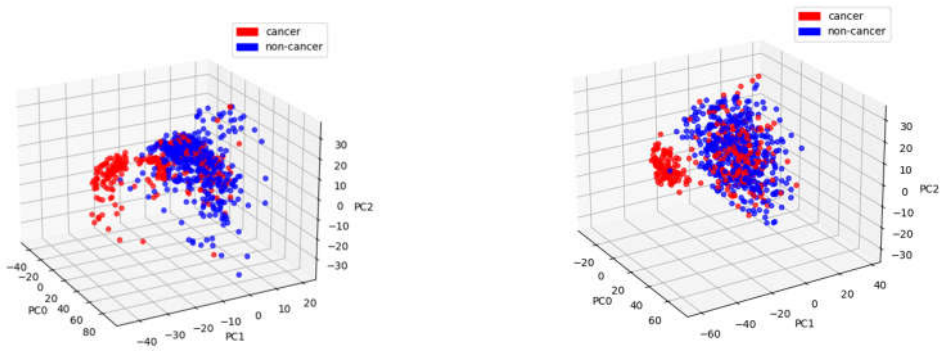

(**a**) (**b**)

Figure 5. PCA-transformed data in 3 dimensions for *2DF*, *LPF*, *STD*, and *Am* with (**a**) *BRF* and (**b**) *BR*.

 doi:10.20944/preprints202411.1739.v2

In both figures, there is a well-pronounced cluster of cancerous samples. However, in Figure 5(a), the points outside this cluster also exhibit a separation. It manifests itself in the metrics. XGBoost provides the AUC of 0.82 and the BA of 0.78 for BRF, while these values are 0.75 and 0.7 for BR.

4. Discussion

Comparing the results obtained by different data preprocessing steps and machine-learning algorithms, we can reveal general trends and make several conclusions:

1. Data representations based on 2D Fourier transformation are vastly superior to their 1D counterparts. This was expected because azimuthal integration eliminates anisotropy, which leads to the loss of information for anisotropic structures, such as keratin.
2. All the classifiers except the Logistic Regression provide similar metrics. We can attribute it to the fact that when there are pronounced clusters, all searching methods would determine them.
3. Reducing the number of Fourier coefficients using the Low-Pass Filter improves diagnostics. Eliminating unimportant features provides a better focus for machine learning algorithms.
4. Removing the area near the primary beam leads to better results. Our custom-developed approach to removing it in the reciprocal space works better than direct removal in the real space.
5. Principal Component Analysis improves the results only with a proper choice of the number of principal components involved. If this number is too small (n = 3) or too large (n = 750), the diagnostics are worse than when n = 50 or 100.
6. All the metrics for patients are much better than those for the samples. This can be expected because averaging the samples belonging to the same patient eliminates the outliers.
7. Our custom procedure to determine 1D Fourier coefficients [20] works better than the standard one.
8. The *KNN* classifier results are the same for 50 and 100 PCs; see lines 9 and 10 of Table 1. In general, the dependence on the PC number is much weaker for *KNN* than for other classifiers.

5. Conclusions

In this paper, we have shown that the data analysis approaches based on Fourier coefficients are beneficial for analyzing anisotropic XRD patterns, especially with 2D transformation. We obtained excellent performance metrics, as for several combinations of the data preprocessing steps and machine learning algorithms, the sensitivity or specificity can reach 1. The best results are achieved by the Random Forest model based on imaginary parts of low-pass-filtered 2D Fourier coefficients with standard scaling, 100 principal components, and the primary beam removed in the reciprocal space. Our methods can be used for canine cancer detection based on the X-ray scans of dog's nails and, in the future, extended to human cancer diagnostics.

Author Contributions: Conceptualization, L.M. and P.L.; methodology, A.A., O.A., S.M., A.L., D.L., and P.L.; software, A.A., O.A., and S.M.; validation, A.A., O.A., L.M., and P.L.; formal analysis, A.A.; investigation, A.A., O.A., S.M., D.Y., A.L., and D.L.; resources, D.Y. and D.L.; data curation, A.A.; writing—original draft preparation, A.A. and L.M.; writing—review and editing, L.M.; visualization, A.A. and S.M.; supervision, P.L.; project administration, D.Y. and P.L.; funding acquisition, D.Y. and P.L. All authors have read and agreed to the published version of the manuscript.

Funding: This research received no external funding.

Data Availability Statement: The files with the XRD patterns for the training and test datasets, as well as the complete table with a set of metrics obtained from different approaches, are available at

Fourier-transformation-based analysis of X-ray diffraction pattern of keratin for cancer detection

The codes are available upon request.

Acknowledgments: We would like to thank the following clinics for providing the samples: Alternative Veterinary Therapies (NY), Animal Medical Center of Seattle (WA), Blue Pearl Veterinary Partners (PA), Bridge Animal Referral Center (WA), Burroughs Veterinary Services (OH), Ethos-WVRC (WI), Evans Family Pet Care

 doi:10.20944/preprints202411.1739.v2

(MN), Intervivo Solutions (ON, Canada), Lakeville Family Pet Clinic (MN), Maryville Small Animal Medical Center (TN), Ocean State Veterinary Specialists (RI), Sen Beevers (CA), Private Veterinary Specialties (NJ), Sage Centers - Campbell & SF (CA), Slaton Animal Hospital (TX), Spay Neuter Veterinary Clinic (NC), Summit Veterinary Referral Center (WA), VCA Sacramento (CA), and Veterinary Specialty Center (IL).

Conflicts of Interest: P.L. is a shareholder of Matur UK, Ltd. and Arion Diagnostics, Inc. D.Y. and D.L. are shareholders of Arion Diagnostics, Inc. A.A., O.A., and S.M. are consultants for Matur UK, Ltd. A.L. and L.M. are consultants for Arion Diagnostics, Inc.

References

1. Siegel, R.L.; Giaquinto, A.N.; Jemal, A. Cancer statistics, 2024. *CA Cancer J Clin.* **2024**, 74, 12–49.
2. Hulka, B. S. Overview of biological markers. In *Biological Markers in Epidemiology*; Hulka, B. S., Griffith, J. D., Wilcosky, T. C., Eds.; Oxford University Press: New York, USA, 1990, pp. 3–15.
3. Naylor, S. Biomarkers: current perspectives and future prospects. *Expert Rev Mol Diagn* **2003**, *3*, 525–529.
4. Henry, N. L.; Hayes, D. F. Cancer biomarkers. *Mol Oncol* **2012**, *6*, 140–146.
5. Passaro, A.; Al Bakir, M.; Hamilton, E. G.; Diehn, M.; André, F.; Roy-Chowdhuri S.; Mountzios, G.; Wistuba, I. I.; Swanton, C.; Peters, S. Cancer biomarkers: Emerging trends and clinical implications for personalized treatment. *Cell* **2024**, *187*, 1617-1635.
6. Friedrich W.; Knipping P.; von Laue M. Interferenz-Erscheinungen bei Röntgenstrahlen. *Sitz. Math. Phys. Classe König. Bayer. Akad. Wiss. München* **1912**, 363.
7. Bragg, W.L. The analysis of crystals by the X-ray spectrometer. *Proc. Royal Soc. London* **1914**, *A89*, 468.
8. Sumner, J. B. The Isolation and Crystallization of the Enzyme Urease. *J. Biol. Chem*. **1926**, *69*, 435–441.
9. Shi, Y.A. Glimpse of Structural Biology through X-Ray Crystallography. *Cell* **2014**, *159*, 995–1014.
10. Denisov, S.; Blinchevsky, B.; Friedman, J.; Gerbelli, B.; Ajeer, A.; Adams, L.; Greenwood, C.; Rogers, K.; Mourokh, L.; Lazarev, P. Vitacrystallography: Structural Biomarkers of Breast Cancer Obtained by X-ray Scattering. *Cancers* **2024**, *16*, 2499.
11. Kidane, G.; Speller, R.D.; Royle, G.J.; Hanby, A.M. X-ray scatter signatures for normal and neoplastic breast tissues. *Phys. Med. Biol.* **1999**, *44*, 1791.
12. Poletti, M.E.; Gonçalves, O.D.; Mazzaro, I. Coherent and incoherent scattering of 17.44 and 6.93 keV X-ray photons scattered from biological and biological-equivalent samples: Characterization of tissues. *X-ray Spectrom.* **2002**, *31*, 57–61.
13. Cunha, D.M.; Oliveira, O.R.; Pérez, C.A.; Poletti, M.E. X-ray scattering profiles of some normal and malignant human breast tissues. *X-ray Spectrom.* **2006**, *35*, 370–374.
14. Moss, R.M.; Amin, A.S.; Crews, C.; Purdie, C.A.; Jordan, L.B.; Iacoviello, F.; Evans, A.; Speller, R.D.; Vinnicombe, S.J. Correlation of X-ray diffraction signatures of breast tissue and their histopathological classification. *Sci. Rep.* **2017**, *7*, 12998.
15. Mohd Sobri, S.N.; Abdul Sani, S.F.; Sabtu, S.N.; Looi, L.M.; Chiew, S.F.; Pathmanathan, D.; Chio-Srichan, S.; Bradley, D.A. Structural Studies of Epithelial Mesenchymal Transition Breast Tissues. *Sci. Rep.* **2020**, *10*, 1997.
16. James, V.; Kearsley, J.; Irving, T.; Amemiya, Y.; Cookson, D. Using hair to screen for breast cancer. *Nature* **1999**, *398*, 33–34.
17. James, V.J. Synchrotron fibre diffraction identifies and locates foetal collagenous breast tissue associated with breast carcinoma. *J. Synchrotron Rad.* **2002**, *9*, 71–76.
18. Briki, F.; Busson, B.; Salicru, B.; Estève, F.; Doucet, J. Breast-cancer diagnosis using hair. *Nature* **1999**, *400*, 226.
19. Suortti, P.; Fernandez, M.; Urban, V. Comments on Synchrotron fibre diffraction identifies and locates foetal collagenous breast tissue associated with breast carcinoma by V. J. James (2002). J. Synchrotron Rad. 9, 71–76. *J. Synchrotron Rad*. **2003**, *10*, 198.
20. Alekseev, A.; Yuk, D.; Lazarev, A.; Labelle, D.; Mourokh, L.; Lazarev, P. Canine Cancer Diagnostics by X-ray Diffraction of Claws. *Cancers* **2024**, *16*, 2422.

 doi:10.20944/preprints202411.1739.v2

21. Schiffman, J. D.; Breen, M. Comparative oncology: what dogs and other species can teach us about humans with cancer. *Philos. Trans. R. Soc. Lond. B Biol. Sci*. **2015**, *370*, 20140231.
22. Gardner, H.L.; Fenger, J.M.; London, C.A. Dogs as a Model for Cancer. *Annu. Rev. Anim. Biosci.* **2016**, *4*, 199–222.
23. Oh, J.H.; Cho, J.-Y. Comparative oncology: Overcoming human cancer through companion animal studies, *Exp. Mol. Med.* **2023**, *55*, 725–734.
24. Lopes, C.K. Canine cancers as models: We have barely tapped the full potential of comparative oncology. *Cancer Lett*. **2024**, *50*, 4.
25. Conceicao, A.L.C.; Meehan, K.; Antoniassi, M.; Piacenti-Silva, M.; Poletti, M.E. The influence of hydration on the architectural rearrangement of normal and neoplastic human breast tissues. *Heliyon* **2019**, *5*, e01219.
26. Pedregosa, F.; Varoquaux, G.; Gramfort, A.; Michel, V.; Thirion, B.; Grisel, O.; Blondel, M.; Prettenhofer, P.; Weiss, R.; Dubourg, V.; Vanderplas, J.; Passos, A.; Cournapeau, D.; Brucher, M.; Perrot, M.; Duchesnay, E. Scikit-learn: Machine learning in python. *J. Mach. Learn. Res.* **2011**, *12*, 2825–2830.
27. https://scikit-learn.org/stable/
28. https://lightgbm.readthedocs.io/en/stable/
29. Chen, T.; Guestrin, C. Xgboost: A scalable tree boosting system. In Proceedings of the 22nd ACM SIGKDD International Conference on Knowledge Discovery and Data Mining, ser. KDD '16. New York, NY, USA: Association for Computing Machinery, 2016, 785–794.
30. https://xgboost.readthedocs.io/en/stable/
31. Wang, B.; Yang, W.; McKittrick, J.; Meyers, M.A. Keratin: Structure, mechanical properties, occurrence in biological organisms, and efforts at bioinspiration, *Prog. Mat. Sci.* **2016**, *76*, 229–318.
32. Sarker, I.H. Machine Learning: Algorithms, Real-World Applications and Research Directions. *SN Comput. Sci.* **2021**, *2*, 160.
33. Moreno, M.; Lytras, M.; Yáñez-Márquez, C.; Salgado Ramirez, J. Classification of Diseases Using Machine Learning Algorithms: A Comparative Study. *Math.* **2021**, 9, 1817.
34. Teixeira, M.; Silva, F.; Ferreira, R.M.; Pereira, T.; Figueiredo, C.; Oliveira, H.P. A review of machine learning methods for cancer characterization from microbiome data. *NPJ Precis. Onc.* **2024**, *8*, 123.
35. Breiman, L. Random Forests. *Machine Learning* **2001**, *45*, 5–32.
36. Bentéjac, C.; Csörgő, A.; Martínez-Muñoz, G. A comparative analysis of gradient boosting algorithms. *Artif. Intell. Rev.* **2021**, *54*, 1937–1967.